Kinetic instabilities in Mercury's magnetosphere: Three-dimensional simulation results

Pavel M. Trávníček,[1,2,3] Petr Hellinger,[1,2] David Schriver,[3] David Herčík,[2] James A. Slavin,[4] and Brian J. Anderson[5]

Received 10 November 2008; accepted 4 February 2009; published 10 April 2009.

[1] A self-consistent global three-dimensional kinetic study of Mercury's magnetosphere is carried out examining waves and instabilities generated by ion temperature anisotropy and plasma flow. The overall structure of Mercury's upstream bow shock and magnetosheath are qualitatively very similar to those of Earth. Beam-generated long-wavelength oscillations are present upstream of Mercury's quasi-parallel bow shock, whereas large-amplitude mirror waves develop downstream of the quasi-parallel bow shock in the magnetosheath. A train of mirror waves forms also downstream of the quasi-perpendicular bow shock. A velocity shear near the magnetopause can lead to formation of vortex-like structures. The magnetospheric cavity close to the planet's equatorial plane is filled with ions much hotter than the solar wind protons. A drift-driven plasma belt close to the equator is present in the model and contains plasma with high-temperature anisotropy, and the loss cone for charged particles in this region is large. The belt may cause diamagnetic effects superimposed on the planet's internal magnetic field and can interact with Mercury's magnetopause. **Citation:** Trávníček, P. M., P. Hellinger, D. Schriver, D. Herčík, J. A. Slavin, and B. J. Anderson (2009), Kinetic instabilities in Mercury's magnetosphere: Three-dimensional simulation results, *Geophys. Res. Lett.*, *36*, L07104, doi:10.1029/2008GL036630.

1. Introduction

[2] Magnetometer data from two flybys of Mercury by the Mariner 10 spacecraft established that the planet closest to the Sun has an intrinsic magnetic field [*Ness et al.*, 1974]. From those observations, Mercury's magnetic dipole moment has been estimated to be between 170 nT R_M^3 ($\approx 2.5 \times 10^{19}$ Am^2) and 349 nT R_M^3 ($\approx 5 \times 10^{19}$ Am^2) [*Connerney and Ness*, 1988]. Here R_M = 2439 km denotes Mercury's radius. Recently, observations by the MErcury Surface, Space ENvironment, GEochemistry, and Ranging (MESSENGER) spacecraft have confirmed the existence of Mercury's magnetosphere and suggested that the strength of the corresponding planetary magnetic dipole is approximately 250 nT R_M^3 [*Anderson et al.*, 2008].

[3] The purpose of this study is to examine the presence of various types of waves triggered by instabilities in Mercury's magnetosphere and magnetosheath, indicate their source, and compare qualitatively to similar phenomena often observed in Earth's magnetosphere. For this study we use the three-dimensional (3-D) hybrid model (i.e., kinetic description of ions, fluid model of electrons) [*Trávníček et al.*, 2007] of the interaction between the solar wind and a planet with a small magnetosphere. To put the simulation results in context we launch a virtual probe along the MESSENGER trajectory, which is useful since it passes through quasi-perpendicular and quasi-parallel bow shocks, the magnetosheath, the magnetospheric cavity, and Mercury's plasma belt, whose existence has been predicted by previous numerical studies by *Delcourt et al.* [2003] and *Trávníček et al.* [2007]. The virtual probe flies by Mercury very near to the planet's equatorial plane. It approaches the planet from the dusk-crossing quasi-perpendicular bow shock and travels through the magnetosheath toward a closest approach to the planet above the night side. Then it exits the planet's magnetosphere through the magnetosheath into the foreshock upstream of the quasi-parallel bow shock. In the following section we describe the initialization of the 3-D hybrid simulation model, the simulation results follow in section 3, and a summary of the analysis and conclusions are presented in section 4.

2. Initialization of the Kinetic Model

[4] We use a 3-D simulation box with 650 × 265 × 265 mesh points distributed along the three (Cartesian) dimensions with the spatial resolution $\Delta x = 0.4\ c/\omega_{pp\mathrm{sw}}$, $\Delta y = \Delta z = c/\omega_{pp\mathrm{sw}} \equiv \Lambda_{p\mathrm{sw}}$, i.e., the size of the simulation domain 260 × 265 × 265 $\Lambda_{p\mathrm{sw}}^3$. Here c is the speed of light, and $\omega_{pp\mathrm{sw}}$ and $\Lambda_{p\mathrm{sw}}$ are the solar wind proton plasma frequency and proton inertial length, respectively. Macro-particles are advanced with the time step $\Delta t = 0.02\ \Omega_{p\mathrm{sw}}^{-1}$ (where $\Omega_{p\mathrm{sw}}$ is the solar wind proton gyrofrequency), whereas the electromagnetic fields are advanced with $\Delta t_B = \Delta t/10$.

[5] We initialize the magnetic field with a superposition of the isotropic interplanetary magnetic field (IMF) and a dipolar planetary magnetic field. The IMF $\boldsymbol{B}_{\mathrm{sw}} = (B_x, B_y, 0)$, $B_{\mathrm{sw}} = 1$, makes an angle $\varphi = -16°$ with respect to the $+X$ axis (i.e., with respect to the solar-wind flow direction). The dipolar field is defined by $\boldsymbol{B}_M = (M/r^3)\ [-2 \sin\lambda\ \boldsymbol{e}_r + \cos\lambda\ \boldsymbol{e}_\lambda]$, where the magnetic moment M and radial distance r from the center of Mercury are non-dimensionalized by $B_{\mathrm{sw}}\Lambda_{p\mathrm{sw}}^3/\mu_0$ and $\Lambda_{p\mathrm{sw}}$, respectively, $\boldsymbol{e}_r$ and $\boldsymbol{e}_\lambda$ are unit vectors in the radial and magnetic latitude directions, respectively, and λ is the magnetic latitude measured from the equatorial plane (X, Y) (no tilt of the planetary dipole

[1] Astronomical Institute, ASCR, Prague, Czech Republic.
[2] Institute of Atmospheric Physics, ASCR, Prague, Czech Republic.
[3] Institute of Geophysics and Planetary Physics, University of California, Los Angeles, California, USA.
[4] Heliophysics Science Division, NASA Goddard Space Flight Center, Greenbelt, Maryland, USA.
[5] John Hopkins University Applied Physics Laboratory, Laurel, Maryland, USA.

0094-8276/09/2008GL036630$05.00

is applied). We use a scaled-down model of Mercury with a magnetic moment $M = 25{,}000\ B_{\rm sw}\Lambda^3_{p\rm sw}\ 4\pi/\mu_0$ (introduced by *Trávníček et al.* [2007]). At $t = 0$ we load the simulation box with 70 macro-particles in each cell (except for the interior of the planet) representing a Maxwellian isotropic proton plasma of density $n_p = n_{p\rm sw} = 1$ with bulk speed $v_p = (v_{\rm sw},0,0)$, where the solar wind speed $v_{sw} = 4\ v_{A\rm sw}$ ($v_{A\rm sw}$ is the Alfvén speed in the solar wind). The ratio of kinetic to magnetic pressure $\beta_{p\rm sw} = 2\ n_{p\rm sw}T_{p\rm sw}/B^2_{\rm sw} = 1$, where $T_{p\rm sw}$ is the solar wind plasma temperature. Electrons have $\beta_e = 1.0$. This plasma flow is continuously injected from the left boundary at $X = -7\ R_M$.

3. Results

[6] We summarize our simulation results in Figures 1, 2, and 3. Figure 1 displays simulated data in various sections of the simulation box, Figure 2 displays data acquired along the trajectory of the virtual probe, and Figure 3 displays the projection of the probe's trajectory onto ($\beta_{p\|}$, $T_{p\perp}/T_{p\|}$) space, where the subscripts denote directions along or perpendicular to the magnetic field. The discussion of results essentially follows the trajectory of the virtual probe.

[7] The spacecraft enters Mercury's bow shock (the first yellow marker "S1") at its dusk side where the shock wave is almost strictly perpendicular, $\beta_p \approx 1$, $T_{p\perp}/T_{p\|} \approx 1$ (see Figure 3a). The increase in the magnetic field at the bow shock causes $T_{p\perp}$ to grow. Downstream of the bow shock the plasma remains marginally stable with respect to the mirror instability (Figure 3a, second yellow marker "S2") forming a downstream wave train of compressible waves (see bow-shock-aligned oscillation of density and magnetic field downstream of the bow shock on Figures 1a–1d and 2g). The train of mirror waves decays further downstream as we approach the white marker "1".

[8] The probe traverses the magnetosheath beyond the marker "1" and enters its expanding region. The convection-driven expansion of the magnetosheath causes $T_{p\perp}$ to grow, however, the plasma anisotropy remains constrained by both the cyclotron and mirror instabilities. This portion of the magnetosheath is indeed filled by (compressible) waves with higher amplitudes (see Figures 1a–1d) and plasma in this region ($\beta_p \approx 1$, $T_{p\perp}/T_{p\|} \approx 1.1$) is marginally stable with respect to both mirror and cyclotron instabilities (Figure 3a). As the probe approaches the magnetopause (the green marker "MI") both $\beta_{p\|}$ and the temperature anisotropy $T_{p\perp}/T_{p\|}$ remain roughly constant (see Figure 3a).

[9] At the magnetopause the plasma density n_p drops as the probe enters the magnetospheric cavity, $v_x \approx 0$, and the plasma temperature increases to the value $\approx 8\ T_{p\rm sw}$; there are still some waves downstream of the magnetopause (see n_p on Figure 1a, v_x on Figure 2c, and $\delta B^2/B^2$ on Figure 2b). Small amplitude wave oscillations downstream of the magnetopause were observed by MESSENGER (Figure 2i). Plasma beta remains at $\beta_p \approx 1$ downstream of the magnetopause, as the density drop has been compensated by the increase in the plasma temperature and the plasma is still nearly isotropic ($T_{p\perp}/T_{p\|} \approx 1.1$, Figure 3b).

[10] After crossing the inbound magnetopause the virtual probe travels through a region with an increased density of magnetospheric plasma (see Figures 1a and 1b). The plasma does not move along the X direction (Figure 2c), magnetic field fluctuations are present in this region (Figure 2b), and the plasma has high beta (Figure 2f). We note that a closer examination of the proton current density and the orientation of the magnetic field suggests that the structure is velocity-shear-driven and its presence close to the magnetopause supports possible formation of vortex-like structures close to Mercury's magnetopause [*Slavin et al.*, 2008]. The plasma density increase in this region causes a diamagnetic drop of the magnetic field (see Figures 1a and 1c), the plasma is hot (Figure 2d), and consequently $\beta_{p\|} \approx 10-11$.

[11] The probe reaches the second white marker "2" where $\beta_{p\|}$ restores its value ≈ 1 and $T_{p\perp}/T_{p\|} \approx 0.7$ (Figure 3b). The magnetospheric plasma in this region flows sunward (Figure 2c). Then the probe continues toward the third white marker "3" located inside Mercury's belt of quasi-trapped particles [*Delcourt et al.*, 2003; *Trávníček et al.*, 2007]. First, as the probe approaches the planet, $\beta_{p\|}$ decreases (Figures 2f and 3b) thanks to the presence of the planetary magnetic field. Once the probe enters the belt, the density increase causes a magnetic field dropout as a result of the diamagnetic effect (Figure 1c) and $\beta_{p\|}$ increases from 0.2 to 0.7 (Figure 3b). Farther down along the spacecraft's trajectory the planetary magnetic field grows and causes $\beta_{p\|}$ to decrease again, first to the value 0.2 at the location of the third white marker "3", then reaching its minimal value 0.015 at closest approach (red marker "CA").

[12] Test particle studies by *Delcourt et al.* [2003] have shown that there is not sufficient magnetic moment to support the formation of a uniform drift-driven current around the entire planet. Examining the direction of the ion current in our model supports this conclusion, as there is not a visibly uniform direction of the proton current circulating the planet. Instead, more likely, Mercury's magnetic field lines act as a temporary trap for charged particles and cause them to bounce at least several times between magnetospheric mirror points before they either hit Mercury's surface or escape into the magnetospheric cavity. Moreover, the mirror points for many of these particles are located below Mercury's surface. Consequently, we expect that velocity distribution functions for Mercury's belt plasma have large pitch angles, causing enhancement of the temperature anisotropy (Figures 2e, 3b, and 3c close to the red marker). Figure 2d suggests that the temperature of the plasma in Mercury's belt may reach values of $10\ T_{p\rm sw}$.

[13] As the virtual probe departs the point of closest approach "CA" toward the outbound green marker "MO", the magnetic field decreases (Figure 1c), causing $\beta_{p\|}$ to grow (Figure 3c). The plasma along the trajectory is again in a marginally stable state with respect to both cyclotron and mirror instabilities and reaches a nearly isotropic state $\beta_{p\|} \approx T_{p\perp}/T_{p\|} \approx 1.1$ at the location of the green marker "MO". The precise location of the outbound magnetopause, however, is somewhat uncertain. The magnetic field itself and its fluctuations (Figures 1c and 2b) suggest that the outbound magnetopause is located at the position of the fourth white marker "4". However, the plasma between location "4" and the green marker "MO" still circulates within the planetary cavity with $v_{px} \approx 0.5\ v_{\rm sw}$ (Figure 2c). This phenomenon can be similar to the double-magnetopause effect reported by *Slavin et al.* [2008] when the magnetopause of Mercury's small magnetosphere

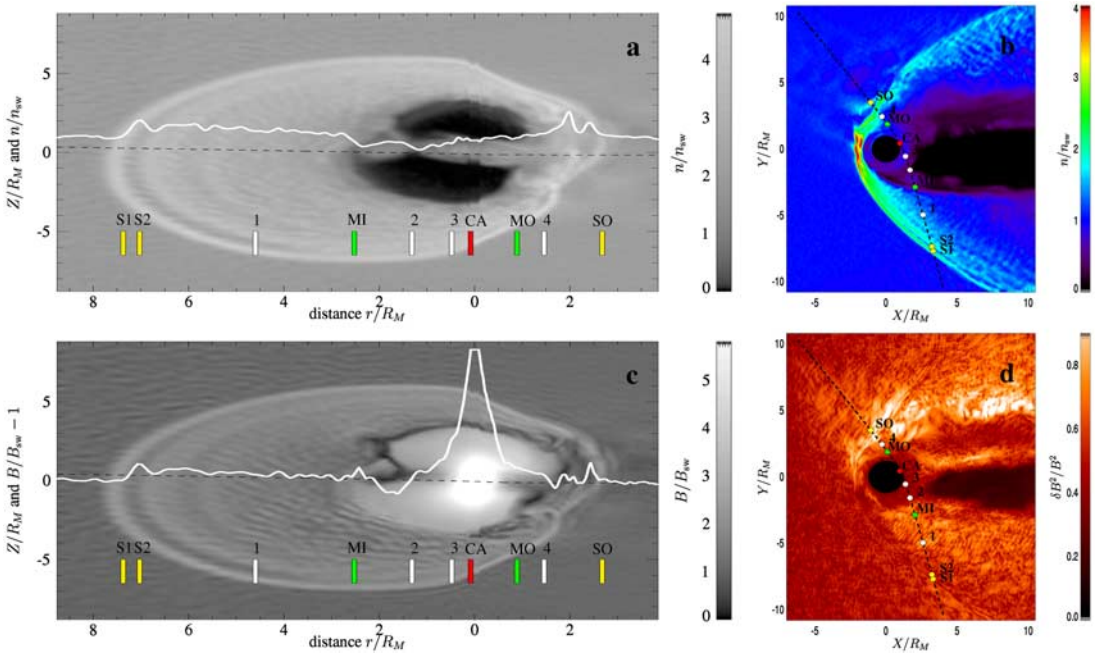

Figure 1. (a and c) Data in two-dimensional sections [$s(X, Y), Z$] of the simulation box, where $s(X, Y)$ is the projection of the spacecraft's trajectory onto the equatorial plane (X, Y). The ticks on the horizontal axis correspond to the distance of the probe from Mercury's surface (altitude). The dashed black horizontal line in Figures 1a and 1c corresponds to the trajectory of the spacecraft projected onto the plane [$s(X, Y), Z$]. Figure 1a displays a gray-shaded plot of the plasma density n/n_{psw} in the plane [$s(X, Y), Z$]. The overplotted solid white line corresponds to the plasma density n/n_{sw} acquired along the trajectory of the virtual probe. The vertical axis corresponds to both density n/n_{sw} and position Z/R_M of the spacecraft with respect to the equatorial plane. Figure 1c displays gray-shaded plot of the magnitude of the magnetic field B/B_{sw}. The overplotted solid white line corresponds to the magnitude of the magnetic field B/B_{sw}-1 acquired along the trajectory of the virtual probe. The vertical axis corresponds to both magnetic field B/B_{sw}-1 and position Z/R_M of the spacecraft. (b) Density n/n_{sw} in the equatorial plane with an overplotted trajectory $s(X, Y)$ of the spacecraft. (d) Estimate of the energy of magnetic field fluctuations $\delta B^2/B^2$ in the equatorial plane with an overplotted trajectory $s(X, Y)$ of the spacecraft. Colored vertical bars in Figures 1a and 1c and corresponding colored bullets in Figures 1b and 1d are used as markers for orientation along the spacecraft trajectory.

interacts with the plasma in Mercury's magnetospheric cavity and causes the development of multiple pressure-balance layers. As the probe crosses the green marker "MO" and flies toward the white marker "4", the magnetic field decreases. That is a necessary consequence of the pressure balance condition maintained at the magnetopause. Upstream of the magnetopause, the magnetosheath plasma bulk flow velocity $v_{px} > 0$ (see Figure 2c) is responsible for a substantial fraction of the upstream plasma dynamic pressure. The plasma temperature drops at the magnetopause (Figure 2d) as well. The plasma remains close to a marginally stable state $\beta_p \approx T_{p\perp}/T_{p\parallel} \approx 1.1$ with respect to the mirror instability close to the white marker "4" (Figures 3c and 3d).

[14] Beyond the white marker "4" the plasma exhibits (compressible) oscillations. These oscillations have the largest amplitudes (Figure 2b) observed during the flyby (see Figure 2i). The density oscillations are anti-correlated with an increase in the plasma temperature (see Figures 1a and 2d). Closer analysis of the trajectory of Figure 3d suggests that the region downstream of the quasi-parallel portion of the bow shock is filled with a cascade of compressed and stretched plasma along the direction of the magnetic field lines. The plasma has high β_p, and there are likely to be waves generated by both mirror and fire-hose instabilities as the plasma changes regimes that are marginally stable with respect to both instabilities (Figure 3b). The large-amplitude mirror waves are relatively robust with respect to dissipation, and they are likely to compete with waves triggered by the fire-hose instability. Moreover, note that this region contains the beam of plasma streaming from Mercury's bow shock back upstream against the solar wind flow, and some waves present in this region can be beam driven. The complexity of the energy exchange between particles and waves in this region is beyond the scope of this letter and deserves a separate detailed study.

[15] Finally, the probe exits Mercury's magnetosheath into Mercury's proton foreshock beyond the outbound yellow marker "SO". Here the parallel temperature is effectively enhanced by the proton beam of plasma traveling upstream from the shock into the proton foreshock. The interaction between the beam and the solar wind plasma causes long-wavelength oscillations in Mercury's proton foreshock.

4. Conclusions

[16] The overall structure of Mercury's upstream bow shock and magnetosheath is qualitatively similar to those of Earth. We observe long-wavelength waves upstream of the quasi-parallel bow shock generated by the interaction

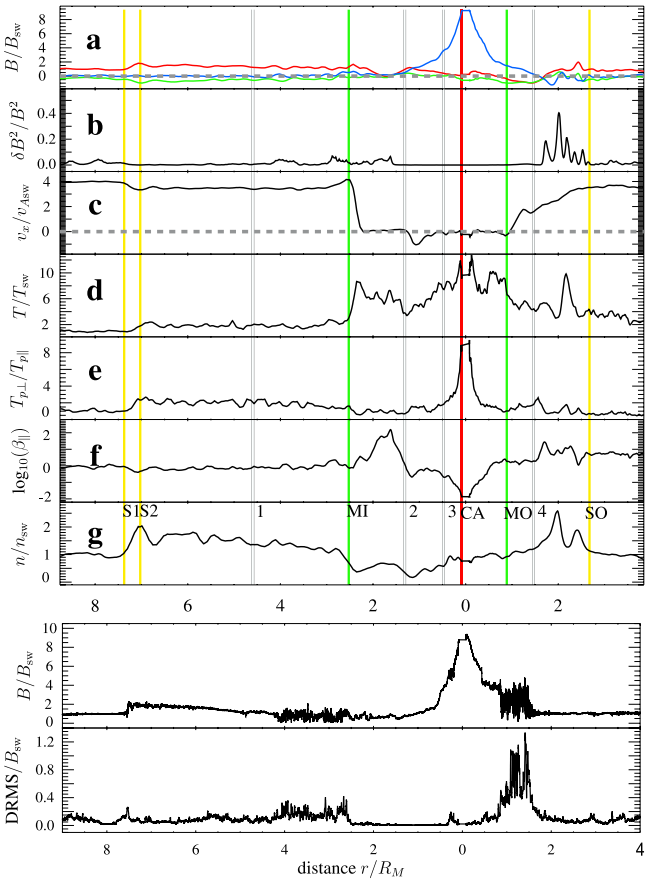

Figure 2. Several observables acquired along the trajectory of the virtual probe: (a) three components B_x/B_{sw} (red), B_y/B_{sw} (blue), B_z/B_{sw} (green) of the magnetic field; (b) estimate of the fluctuating energy of the magnetic field $\delta B^2/B^2$; (c) X-component v_x/v_{Asw} of the plasma bulk velocity; (d) plasma temperature $T/T_{psw} = 1/3\ (T_{p\parallel} + 2T_{p\perp})/T_{psw}$; (e) temperature anisotropy $T_{p\perp}/T_{p\parallel}$; (f) $\log_{10}(\beta_\parallel) = \log_{10}(2nT_{p\parallel}/B^2)$; and (g) density n/n_{sw}. The horizontal gray dashed line on Figures 2a and 2c marks the zero value. Also shown are (h) magnetic field B/B_{sw} acquired by MESSENGER during its first flyby of Mercury and (i) its standard deviation $\mathrm{DRMS} = \sqrt{\frac{1}{N}\sum_i (\mathbf{B}_i - \overline{\mathbf{B}})^2}/B_{sw}$.

between the backstreaming beam of magnetosheath plasma and the solar wind. Downstream of the quasi-perpendicular bow shock we observe a train of mirror waves. Large-amplitude mirror waves also form downstream of the quasi-parallel bow shock. A cascade of domains with magnetic compression and expansion along the magnetic field lines is characteristic for this region, and our results suggest that waves produced by the beam and/or fire-hose instability are present in this region of Mercury's magnetosheath. Our results also suggest that velocity-shear-driven vortex-like structures can develop close to the (inbound) magnetopause, possibly similar to those observed by *Slavin et al.* [2008]. In our case these structures contain plasma of high $\beta_p \approx 10$.

[17] The magnetospheric cavity is filled with less dense, hotter plasma with a plasma temperature $T_p \sim 8-10\ T_{psw}$. Previous work by *Delcourt et al.* [2003] and *Trávníček et al.* [2007] predicts that a drift-driven belt of quasi-trapped particles forms close to Mercury's surface. Thanks to the small magnetic moment of Mercury's magnetic field, the loss cone for charged particles in this region is large and the ions with pitch angle within the loss cone hit Mercury's surface. In effect, the loss of ions to the surface reduces further the parallel temperature of the ion distribution. The plasma close to Mercury can cause development of diamagnetic signatures superimposed on the planetary magnetic field. Also, magnetospheric plasma close to the equatorial plane can reach Mercury's magnetopause and can potentially lead to the development of multiple pressure-balance layers [*Slavin et al.*, 2008].

[18] Simulation results presented in this letter are limited by the use of the downscaling technique [*Trávníček et al.*, 2007] and/or finite spatial resolution that can not resolve thin boundaries. However, some of our simulation results are in general qualitatively similar to the observations by the MESSENGER spacecraft, namely the relative amplitude of wave oscillations in the magnetosheath and downstream of the quasi-parallel bow shock, possible development of velocity-shear-driven structures close to the inbound magnetopause, and development of multiple pressure balanced layers downstream of the outbound magnetopause [*Anderson*

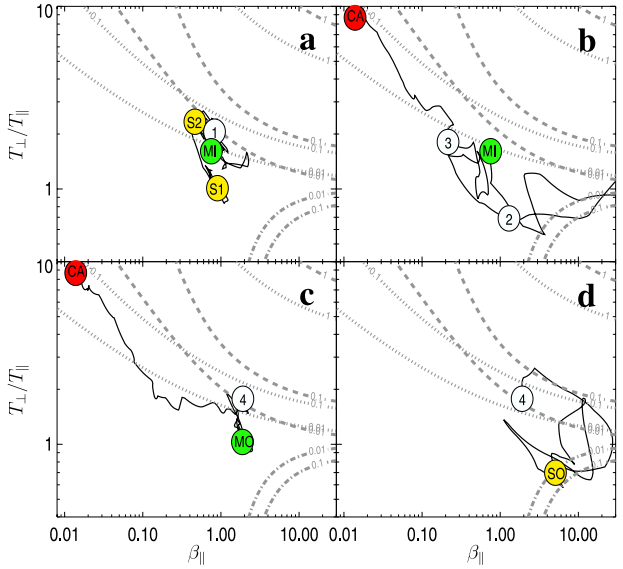

Figure 3. Projections of the probe's trajectory onto ($\beta_{p\parallel}$, $T_{p\perp}/T_{p\parallel}$) space. (a) The probe traverses the inbound bow shock between points "S1" (isotropic plasma with $\beta_\parallel = 1$) and "S2". Then it continues through point marked by the white marker "1", as it moves toward the inbound magnetopause (green marker "MI"). (b) The spacecraft continues through points marked by white markers "2" and "3" and reaches the point of closest approach (red marker "CA"). The spacecraft (c) reaches the outbound magnetopause (green marker "MO" and the white marker "4") and (d) travels through the bow shock (yellow marker "SO") into the proton foreshock. Gray lines display isocontours of the maximal growth rates of three temperature-anisotropy-driven instabilities as predicted by the linear theory for a bi-Maxwellian plasma. Isocontours of growth rate levels of proton mirror, proton cyclotron, and proton fire-hose instabilities are marked by dotted, dashed, and dash-dotted lines, respectively.

et al., 2008; *Slavin et al.*, 2008]. Our study also does not include heavy ions, such as sodium Na^+, observed at Mercury. Transport of heavy ions is usually studied by Monte-Carlo (i.e., not self-consistent) techniques [e.g., *Delcourt et al.*, 2003] as gyroperiods of these ions are much higher than those of protons and require much longer simulation times.

[19] A magnetosphere (even a virtual one), is obviously a complex system. Many issues raised in this letter warrant additional, more detailed studies.

[20] **Acknowledgments.** Authors acknowledge the support of contract 300030805 from the Grant Agency of the Academy of Sciences of the Czech Republic (ASCR), ESA PECS contract 98068 from the European Space Agency, and NASA MESSENGER Participating Scientist grant NNX07AR62G. This work has been performed on the Amalka supercomputing facility, Institute of Atmospheric Physics, ASCR. Part of this work has been supported by Post Rouge, CNRS, France, awarded to PT.

References

Anderson, B. J., M. H. Acuña, H. Korth, M. E. Purucker, C. L. Johnson, J. A. Slavin, S. C. Solomon, and R. L. McNutt Jr. (2008), The structure of Mercury's magnetic field from MESSENGER's first flyby, *Science*, *321*, 82–85.

Connerney, J. E. P., and N. F. Ness (1988), Mercury's magnetic field and interior, in *Mercury*, edited by F. Vilas, C. R. Chapman, and M. S. Matthews, pp. 494–513, Univ. of Ariz. Press, Tuscon, Ariz.

Delcourt, D. C., S. Grimald, F. Leblanc, J.-J. Berthelier, A. Millilo, A. Mura, S. Orsini, and T. E. Moore (2003), A quantitative model of the planetary Na^+ contribution to Mercury's magnetosphere, *Ann. Geophys.*, *21*, 1723–1736.

Ness, N. F., K. W. Behannon, R. P. Lepping, Y. C. Whang, and K. H. Schatten (1974), Magnetic field observations near Mercury: Preliminary results from Mariner 10, *Science*, *185*, 151–160.

Slavin, J. A., et al. (2008), Mercury's magnetosphere after MESSENGER's first flyby, *Science*, *321*, 85–89.

Trávníček, P. M., P. Hellinger, and D. Schriver (2007), Structure of Mercury's magnetosphere for different pressure of the solar wind: Three dimensional hybrid simulations, *Geophys. Res. Lett.*, *34*, L05104, doi:10.1029/2006GL028518.

B. J. Anderson, John Hopkins University Applied Physics Laboratory, Laurel, MD 20723-6099, USA. (brian.j.anderson@jhuapl.edu)

P. Hellinger, D. Herčík, and P. M. Trávníček, Institute of Atmospheric Physics, ASCR, Bocni II/1401, 14131 Prague 4, Czech Republic. (petr.hellinger@ig.cas.cz; trav@ig.cas.cz)

D. Schriver, Institute of Geophysics and Planetary Physics, University of California, Los Angeles, CA 90095-1567, USA. (dave@igpp.ucla.edu)

J. A. Slavin, Heliophysics Science Division, NASA Goddard Space Flight Center, Greenbelt, MD 20771, USA. (james.a.slavin@nasa.gov)